Nanoscale

Accepted Manuscript

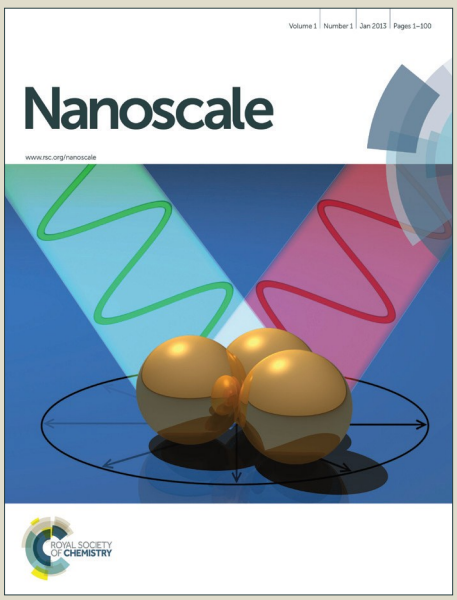

ROYAL SOCIETY OF CHEMISTRY

www.rsc.org/nanoscale

Nanoscale Structure and Superhydrophobicity of sp^2-Bonded Boron Nitride Aerogels

Thang Pham[†a,b,c,i], Anna P. Goldstein[†a,d,i], James Lewicki[e], Sergei O. Kucheyev[e], Cheng Wang[f], Thomas P. Russell[g,h], Marcus A. Worsley[e], Leta Woo[e], William Mickelson[a,c], and Alex Zettl[a,c,h,i*]

Aerogels have much potential in both research and industrial applications due to their high surface area, low density, and fine pore size distribution. Here we report a thorough structural study of three-dimensional aerogels composed of highly crystalline sp^2-bonded boron nitride (BN) layers synthesized by a carbothermic reduction process. The structure, crystallinity and bonding of the as-prepared BN aerogels are elucidated by x-ray diffraction, ^{11}B nuclear magnetic resonance, transmission electron microscopy, and resonant soft x-ray scattering. The macroscopic roughness of the aerogel's surface causes it to be superhydrophobic with a contact angle of ~155^o and exhibit high oil uptake capacity (up to 1500 wt%). The oil can be removed from the BN aerogel by oxidizing in air without damaging the crystalline porous structure of the aerogel or diminishing its oil absorption capacity.

Introduction

Porous materials such as zeolites, silica gels, and inorganic oxides are attractive because of their unique three-dimensional structure and rich chemistry.[1–3] These materials are immensely useful in applications such as gas adsorption, filtration, catalysis, electronics, and energy storage. [4,5] Recently, the synthesis and characterization of porous boron nitride (BN) materials have been reported.[6–8] Boron nitride is chemically inert, thermally stable, and highly thermally conducting,

while electrically insulating. These attributes make BN-based porous materials potentially very useful for applications such as chemical filtration, pollutant absorption, and gas storage.

Porous BN materials have been synthesized by (1) reacting complexes of boron oxide and organic amines with nitrogen-containing gases[6,8] or (2) carbothermic conversion of graphene aerogels via a vapor phase reaction with boron oxide and nitrogen gas.[7] Porous BN materials produced by method 1 exhibit high surface area, which has been exploited for hydrogen storage and oil adsorption, and tend to be superhydrophobic. In comparison to porous BN synthesized by method 1, the porous BN aerogels produced by method 2 exhibit a high degree of crystallinity, in addition to having moderately high specific surface area. Until now, it was unknown how the degree of crystallinity affects the surface properties and absorption capacity of porous BN.

In this report, the crystal structure, chemistry, surface properties, and oil absorption capacity of BN aerogels synthesized via the carbothermic reduction process (method 2) are systematically described. BN aerogels exhibit a primarily turbostratic structure of arbitrarily stacked yet highly crystalline sp^2-bonded BN layers as evidenced by x-ray diffraction (XRD) and transmission electron microscopy (TEM). The local chemical structure of the BN aerogels is characterized by ^{11}B nuclear magnetic resonance (NMR) and the orientation of the BN layers around the pores is probed by resonant soft x-ray scattering (RSoXS). Finally, the surface properties are characterized using water contact angle (WCA) measurements and the oil absorption/adsorption properties are investigated.

Experimental

Synthesis of sp^2-bonded BN aerogels. Boron oxide powder (Alfa Aesar) is loaded into a cylindrical graphite crucible. The graphene aerogels are synthesized by the previously published

method[9] and placed in the middle of the crucible in a separate graphite sample holder. The center and the bottom of the sample holder are perforated with small holes to ensure the adequate flow of reactant vapors. The crucible is then heated to 1600-1800 °C by a radio frequency induction furnace under 2000 sccm flow of N_2 gas. The N_2 gas is flowed through a center tube to the bottom of the crucible, where it mixes thoroughly with boron oxide vapor before reacting with the graphene aerogels. Ref. 7 includes more synthetic details, including a schematic of the reaction chamber.

TEM and XRD characterization. Aberration-corrected TEM images are collected using the TEAM I microscope (National Center for Electron Microscopy at Lawrence Berkeley National Laboratory) operating at 80 kV. Low-resolution TEM is performed on a JEOL 2010 microscope at 80 kV. Powder X-ray diffraction patterns are collected on a Bruker D8 Advance diffractometer with Cu-Kα radiation.

NMR. All ^{11}B solid state NMR analyses are carried out on a Bruker Avance III NMR spectrometer operating at a 600 MHz ^{1}H Larmor frequency and using a Bruker 1.3mm Very Fast Magic Angle Spinning (MAS) broadband – ^{1}H/D probe. 10 mg samples are powdered and packed into 1.3 mm zirconia rotors. ^{11}B spectra are obtained using a standard solid echo sequence optimized for ^{11}B with at sample spinning rates of 55 kHz, using a 90° pulse length of 1 μs at 10 Watts and a recycle delay of 10 seconds. All ^{11}B spectra are referenced to a trimethylborate (TMB) standard. For comparison with the BN aerogel, h-BN powder with a purity of >99% obtained from M K Impex, Canada, is analyzed.

Nanoindentation. Samples are indented at room temperature in the load-controlled mode in an MTS XP nanoindenter with a spherical sapphire indenter with a radius of 496 μm. A series of

partial indents with multiple load-unload cycles (with complete unloading) are performed. Both loading and unloading rates are kept constant to maintain an indentation strain rate of 10^{-3} s^{-1}.[10] Young's modulus (E) and indentation stress (average contact pressure) are calculated based on the initial slope of the unloading curve according to the Oliver-Pharr method.[11] Indentation stress-strain curves are derived from spherical indentation load-displacement data as described previously.[10]

Resonant Soft X-ray Scattering (RSoXS). experiments are conducted at the Advanced Light Source, Beam Line 11.0.1.2.[12] BN aerogel samples are sonicated in isopropanol and drop-cast onto silicon nitride membranes (Norcada). The beamsize is 100 μm x 100 μm. RSoXS data are collected in transmission geometry using an in-vacuum CCD camera using different photon energies near the Boron K-edge (~191 eV), Carbon K-edge (~285 eV) and Nitrogen K-edge (~400 eV). Both horizontally S and vertically P polarized x-rays are used to identify scattering anisotropy caused by the local molecular ordering. RSoXS data are reduced using SAXS analysis software Nika.[13]

Contact angle measurement. The contact angle measurement is carried out by a static sessile drop method using a 10 μL drop of deionized water. Five different positions on the aerogel sample are examined using a Rame–Hart Model 290 Automated Goniometer equipped with DROPimage Advanced analysis software. In each measurement, the static contact angle between the aerogel and the liquid droplet is computed by defining the interfaces of solid/liquid and liquid/vapor. Both angles from the left and the right sides of the droplet are measured and then averaged.

Results and Discussion

A previous study[7] showed that graphene aerogels produced by method 2, the carbothermal conversion process, are fully converted to sp^2-bonded BN. There are two distinct crystal structures of sp^2-bonded BN: hexagonal (h-BN) and rhombohedral (r-BN). These two crystal structures differ in the registry between the sp^2-bonded layers of BN, as shown in Fig. 1a. Another related structure is turbostratic BN (t-BN), where there is no particular ordering between the sp^2-bonded layers. In order to identify the crystal structure of the BN aerogel, we performed X-ray diffraction (XRD).

Fig. 1b shows XRD patterns of the BN aerogel (upper, red) and the starting graphene aerogel (lower, blue). The graphene aerogel precursor material has very broad XRD peaks, characteristic of an amorphous material.[9,14,15] The BN aerogel XRD data show two features. The first feature is a peak centered at 25.8° corresponding to the interlayer spacing between the sp^2-bonded BN of approximately 3.45 Å. The second feature is a broad, tailing peak with its maximum at 41.5° corresponding to the intralayer $(10\bar{1}0)$ planes.[16] The absence of a distinguishable $(10\bar{1}1)$, as would be expected for h-BN or r-BN, indicates that there is no appreciable long-range ordering of the registry between the BN layers. Therefore, the BN aerogel is primarily t-BN[17,18], yet is comprised of highly crystalline sp^2-bonded atomic layers.

Although there is no clear registration of the BN layers, XRD indicates that the individual atomic layers themselves are highly crystalline. We probe the chemical bonding environment within the atomic sheets of the BN aerogel using ^{11}B nuclear magnetic resonance (NMR). From the ^{11}B NMR data, shown in in Fig. 1c, we see that the electronic environment of the boron is very similar to that of the h-BN control sample; *i.e.* a single repeating BN_3 unit structure, as evidenced by the similar line shapes and chemical shifts of 24.1 and 22.1 ppm in the BN aerogel and h-BN control, respectively. These features are consistent with those reported by Marchetti *et al.* for h-

BN.[19] These data indicate that the intralayer bonding structure of the sp^2-bonded BN is highly crystalline and indistinguishable from bulk h-BN.

XRD indicates no appreciable long-range preferred stacking orientation of the BN layers within the BN aerogel. However, there could be preferred short-range translational and/or rotational order within the material. In order to probe the short-range stacking relationship between atomic layers, the BN aerogel is characterized by TEM. Fig. 2a and 2b show conventional TEM images of BN aerogels. These images corroborate XRD and NMR data indicating highly crystalline sp^2-bonded BN sheets, as evidenced by the high contrast, straight walls corresponding to areas where the atomic layers lie parallel to the electron beam. To determine the relative orientation of these atomic sheets with respect to their neighbors, aberration-corrected TEM is employed. Fig. 2c shows an aberration-corrected TEM image of a BN aerogel. This image contains many areas where the sheets lie perpendicular to the beam and areas where the sheets are parallel to the electron beam, which appear as bright lines of alternating contrast. Both orientations give new information regarding the crystal structure of the BN aerogel.

Fig. 2d shows a zoomed-in view of an area where the layers are perpendicular to the electron beam. A Moiré pattern is observed due to the constituent atomic layers being rotated with respect to one another. A fast Fourier transform (FFT) of the image shown in Fig. 2d reveals five distinct hexagonal patterns, with a spacing of 0.22 nm. This distance corresponds to the $(10\bar{1}0)$ spacing of a single sp^2-bonded BN layer. The angles between these spot patterns appear to be arbitrary (relative to one chosen spot, the other four appear at 2°, 31°, 34°, and 39°). The analysis of Fig. 2d is representative of results from other segments of the BN aerogel. For additional examples of rotational misorientation among layers of BN, see Fig. SI1† and SI2†. There are also some sheets that display only a single hexagonal pattern, indicating that while not predominant, there are

regions of rotationally ordered stacking of h-BN (Fig. SI3†). However, most of the analyzed segments of the aerogel displayed a concurrence of multiple spot patterns, which suggests t-BN and corroborates our findings from XRD.

Analysis of aberration-corrected TEM images of areas where the atomic layers lie parallel to the electron beam gives a different point-of-view on the relationship between BN layers. Fig. 2e shows a zoomed-in view of seven BN atomic layers that lie perpendicular to the electron beam. The top five layers have a zone axis that is parallel to the electron beam. This alignment produces a high contrast pattern within the layer, as plotted in Fig. 2f. Based on the intralayer spacing of 0.21-0.22 nm for these five layers, we infer that the bright spots are overlapping stacks of B and N atoms within the same layer. Meanwhile, the two layers at the bottom of the sheet yield a low contrast pattern and cannot be assigned a lattice spacing. We conclude that these bottom two sheets have a rotational orientation with no zone axis parallel to the electron beam, so they are not able to be atomically resolved at this viewing angle.

Since the top five layers in Fig. 2e are similarly rotationally oriented, we can use the register shift between them to understand the type of stacking present in this segment. In terms of atom placement in the hexagonal lattice, h-BN exhibits no shift between adjacent sp^2-bonded layers, whereas each adjacent layer of r-BN (Figure 1a) is shifted by 33% of the lattice parameter in the $[10\bar{1}0]$ direction. The shifts observed between adjacent layers in this sheet are -2%, -25%, 27, and 11%, as shown in Fig. 2g, indicating no consistent translational relationship between the layers. This is further supporting evidence that the BN sheets are neither exclusively ordered h-BN nor r-BN, but are in fact largely t-BN with different degrees of rotational and translational ordering across the sample. The high degree of misorientation between adjacent layers is not surprising. Even if the atomic layers of a particular segment of the aerogel were aligned, the

atomic layer would become misaligned traversing a bend in the aerogel sheet. Since the path lengths across a bend would be different for each layer, the registry between the layers would become disturbed, even for a segment of pristine sp^2-bonded BN layers.

Analysis of TEM images indicates that the BN aerogels have a nanoporous structure with the sp^2-bonded layers lying parallel to the pores. However, since TEM is not well suited for bulk characterization, the physical structure of the BN aerogel is additionally characterized by resonant soft x-ray scattering (RSoXS). RSoXS is an x-ray scattering method using soft x-rays near the absorption edge that provide elemental/chemical sensitivity. It offers statistical information of morphological heterogeneity over a large sample area (100 μm × 100 μm) and covers a broad size scale (nm-μm). With polarized x-rays, RSoXS is sensitive to the molecular bond orientation, especially local molecular orientation that cannot be observed with other methods.[20–22] The RSoXS data give new information on the size and composition of the aerogel's pores before and after conversion to BN. As shown in Fig. 3a, the graphene aerogel has a broad scattering feature centered at ~0.035 A^{-1}, which corresponds to a distribution of real space structure of 18 nm, and we assign this to the average wall-to-wall distance for the porous structure. The BN aerogel shows a scattering feature at ~0.023 A^{-1}, which corresponds to an average wall-to-wall distance of 27 nm. The increased pore size for BN confirms our observations by TEM, as well as nitrogen adsorption porosimetry, wherein the isotherm for the BN aerogel displayed hysteresis at a higher relative pressure.[7] This expansion may be a consequence of the conversion mechanism,[23] wherein boron and nitrogen substitute for carbon. At high temperature, this substitution drives out atomic defects and increases crystallinity within the sheets. As the sheets become less wrinkled and more flat, the pores that they encase grow larger.

Resonant scattering anisotropy is observed near the boron K-edge for BN samples and carbon K edge for graphene samples, as shown in Fig. 3b. This scattering anisotropy does not depend on the sample orientation, but is caused by the local bonding orientation at the surface. This is an indication that an ordered bonding structure is present within the walls of the porous aerogel. X-rays at resonant energies only interact with the bonds that are perpendicular to the electric field of x-rays, and therefore the scattering becomes anisotropic. The scattering contrast between the walls and the pores changes as a function of x-ray photon energy. For the BN aerogel, the scattering anisotropy is most significant near the boron K-edge (191 eV) and is also observed for the nitrogen K-edge. The strong 1s-π^* resonance at ~191 eV does not appear in sp^3-bonded BN, thus demonstrating that the BN in the aerogel is sp^2-bonded.[24] This result agrees well with the TEM and XRD data. For the graphene aerogel, the scattering anisotropy is visible near the carbon K-edge (285 eV), which is also from 1s-π^* resonance, while it is completely isotropic at the boron and nitrogen edges (data not shown). The structure of h-BN is known to be similar to graphite, which explains the similar anisotropy of scattering observed. The anisotropic response from RSoXS demonstrates that the atomic layers lie parallel to the vacuum-aerogel interface, i.e., the π orbital of graphene or h-BN is perpendicular to the vacuum-aerogel interface. The bonding environment of atoms in the graphene/BN aerogel is anisotropic along the surface of the pore, such that the layers of graphene/BN sheets are wrapped around the pore walls rather than being stacked perpendicular to the interface. If the sp^2-bonded BN layers were aligned radially outward from the pores, the scattering anisotropy would be perpendicular to the electric field polarization. Since the scattering anisotropy is parallel to the electric field of the x-rays, the aerogels are mostly comprised of sheets lying parallel to the pores. This confirms that the nanoscale

characterizations of the aerogel by TEM are representative of the nanoscale morphology throughout the entire sample.

It is well known that the Young's modulus of porous nanomaterials depends superlinearly on monolith density, ρ, with an exponent typically between 2 and 4.[25] The mechanical properties of the BN aerogels are characterized by spherical nanoindentation. Fig. 4 shows load-displacement and the corresponding stress-strain curve for a BN aerogel with a density of 60 mg/cm^3. The stress-strain curve corresponds to a Young's modulus of 1.6 MPa. For graphene aerogels, the Young's modulus' dependency on density goes as $\rho^{2.5}$, and graphene aerogels of the same density as the BN aerogel measured here have a Young's modulus of approximately 6 MPa [25]. Since graphite and h-BN have similar Young's moduli[26], the increase in compliance of BN aerogels compared to graphene aerogels indicates a larger exponent of the density dependence of the modulus. A reason for this can be related to the conversion process itself. It has been shown that the mechanical stiffness of carbon aerogels depends highly on the degree of cross-linking.[27] Upon the carbothermic reduction process, carbon atoms in graphene lattice sites will undergo the conversion to BN.[7] During this conversion process, there will be intermediate states as the material is converted form carbon to BN. When carbon atoms located in the cross-links between graphene sheets undergo conversion, the converted boron or nitrogen atom can either be incorporated into the sp^2-bonded BN sheet or remain as a cross-link between the BN sheets. Since it is energetically favorable for an atom to be incorporated into the newly formed BN layers rather than remain in the higher energy state as a crosslinking atom[28], many of the cross-links that originally existed in the graphene aerogel will be removed during the conversion process, thereby decreasing the modulus of the material. In addition to being more compliant, the BN aerogels also exhibit more energy dissipation than graphene aerogels[25], as seen in the large

hysteresis in the load-unload cycle, which could be attributed to the BN sheets sliding past each other causing energy to be lost via friction.

Fig. 5 shows a typical SEM image of the BN aerogel. The sp^2-bonded BN sheets wrapping around the pores form the rough surface of the aerogel. In order to characterize the interaction of this hierarchical structure with water, its wettability is determined via contact angle measurements. The converted BN aerogels are nominally superhydrophobic, with a contact angle of 155° ± 3°, as presented in the inset of Fig. 5. Interestingly, other experimental studies suggest that flat, smooth homogeneous h-BN films are quite hydrophilic,[29,30] presumably due to the ionic character of the B-N bond, which enhances its interaction with polar water molecules. This then begs the question of why converted BN aerogels are superhydrophobic.

One possibility is that the inherently rough surface morphology of BN aerogels influences its interaction with water. Such a structural contribution to hydrophobicity is well known for a variety of systems, for example the mottled surface of the stenocara beetle of the Namib desert[31]. Another is that foreign molecular species adsorbed on the BN aerogel surface from the ambient environment post-synthesis alter the local chemistry and hence wettability, as has been proposed for BN nanotubes and vertically aligned BN nanosheets[32–36]. In order to examine in greater detail relative contributions of these effects, we examine competing wetting models along with a series of detailed post-synthesis surface treatments including high temperature anneals in air or inert environments, and plasma treatments.

To analyze wetting characteristics, two models, Wenzel[37] and Cassie-Baxter[38], are often considered[32,36]. In the Wenzel model, the water conformally wets, and is pinned by, the

rough surface. For our BN aerogels, however, the water droplet easily rolls off the surface at a small tilt angle, apparently rendering the Wenzel model inapplicable. In the Cassie-Baxter model the water droplet can bridge over the composite surface and air pockets instead of filling the rough surface, leading to hydrophobicity. Interestingly, the potentially strong interaction between water and h-BN[30] sets an upper limit of 90^o on the contact angle, well below our measured contact angle of 155^o. We therefore examine possible molecular absorption effects, which have also been used to explain time-dependent wettability experiments for graphene[36], via post-synthesis surface cleaning/functionalization through heat and plasma treatment.

As synthesized BN aerogels are subjected to three independent treatments: (i) thermal annealing for 1 hour under inert Ar flow at 700 and 800 °C; (ii) thermal annealing in air for 1 hour at 700 °C; and (iii) UV – ozone plasma cleaning for different time periods: 15 mins, 60 mins and 90 mins. The results, summarized in Table 1 and illustrated in Fig. SI4†, are as follows: After inert gas annealing (treatment (i)), the WCA is largely unchanged, remaining close to 155^o, and superhydrophobicity persists. Inert gas annealing serves to partially remove possible organic absorbents, but the BN aerogel surface is rough and has a high surface area, which promotes quick re-absorption of organic contaminants (the XPS spectrum of BN aerogel shows C 1s peak with C/B ratio of 0.3) and a reemergence of hydrophobicity. Such readsorption could happen in matter of few seconds immediately after taking the samples out of oven before transferring them into the WCA instrument. Samples annealed in air (treatment (ii)) have a dramatically different behavior. The WCA is initially reduced to <90^o, and, even after several days' exposure to air (and hydrocarbons in the air) to WCA never exceeds 98^o. The samples become hydrophobic, but not

superhydrophobic. A similar and even more severe behavior is observed for plasma-treated samples. Following UV–ozone plasma treatment for 90 minutes, the WCA is close to 60^{o}. After additional exposure to air, the WCA increases over time, but it never returns to the original value of 155 °. After 4 days, the WCA increases and then saturates at 125°, 94°, and 92° for the 15, 60 and 90 - minute – treated samples, respectively. Detailed SEM analysis shows that the surface of BN aerogels is significantly altered by UV–ozone plasma: the surface becomes much flatter in comparison to that of the as–synthesized BN aerogels, and, even with hydrocarbon contamination from the environment, the WCA saturates near 90^{o}. We conclude that the thermodynamically stable superhydrophobic state of BN aerogels likely comes from a combination of hierarchical structure and spontaneous deposition of organic contaminants on freshly synthesized BN aerogels. The discussion in refs. 6, 32 and 36 and the data on superoleophilicity of BN aerogels as presented below support this assumption.

To determine whether the BN aerogel is oleophobic in addition to being superhydrophobic, such as in the case of polytetrafluoroethylene, it is brought into contact with various oils. In stark contrast to the case with water, oils completely wet the BN aerogel and are readily absorbed into the material. To determine the level of oil uptake, five different types of oil are exposed to the BN aerogel: kerosene, white gas, linseed oil, vacuum pump oil, and heavy white mineral oil. For each experiment, the BN aerogel is first weighed, then soaked in the oil for one minute, and finally re-weighed. The BN aerogel is capable of absorbing up to 1500% of its mass in a matter of minutes (Fig. 6a). This absorption capacity is higher than that of commercial activated carbon[39] and comparable to other reported high-performance absorbents, such as graphene hydrogels,[40] graphene capsules,[41] and polyurethane sponge.[42] After 1 min the BN aerogel oil

uptake is nearly complete. To verify this, the aerogels are left to soak for 3 hours and then weighed again for comparison. The mass of oil-soaked aerogels only increases by 1% after an additional 3 hours soak. Fig. SI5† shows photos of pump oil floating on a water bath before and after introducing BN aerogel.

Oil-soaked aerogels can be regenerated by burning in air at 650 °C for 2.5 hours using a conventional tube furnace. The aerogel is restored to its original white color following regeneration. The mass of the aerogel after regeneration increases less than 1% and subsequent oil uptake is over 95% of the original value, both of which are within the experimental error of the measurement, indicating negligible damage to the BN aerogel after regeneration. The BN aerogels can also be regenerated by igniting the trapped oil with an open flame and thereafter still retain over 93% of their original oil uptake capacity. The small difference in mass uptake after the different regeneration methods speaks to the excellent thermal stability and robustness of the BN aerogel. In fact, the microstructure of the as-synthesized BN aerogels after burning at 650 °C or using a flame are both indistinguishable from the original BN aerogels, as seen in Figure 6b. Thermal gravimetric analysis (TGA) data of the BN aerogel are shown in Fig. SI6†, which clearly show thermal stability up to 1000 °C.

Previous studies on the oil adsorption of porous BN nanostructures[6] proposed three potential mechanisms of oil adsorption: i) adsorption of molecules on the hydrophobic BN surface, ii) capillary effect of filling the pore and the space between the sheets, and iii) intercalation of molecules into the interplanar space between BN layers. To determine which mechanism is responsible, the authors of ref. 6 performed XRD on the porous BN material before and after oil absorption. Prior to oil adsorption, they observed a diffraction peak at 26° from the (0002) lattice spacing in BN. After oil absorption, they observed a broad peak near 18°, which they attributed

to an increase in the (0002) BN lattice spacing to approximately 4.8Å, due to oil intercalation between the BN atomic layers. The BN aerogel materials presented here are also characterized by XRD and a similar change in the diffraction pattern is observed before and after oil absorption. However, TEM analysis after oil absorption does not show any evidence of (0002) lattice expansion. To determine the root of the broad peak observed near 20°, XRD is performed on a droplet of mineral oil on a copper foil (see Fig. SI7†). Interestingly, the XRD pattern shows a broad peak centered at 18 °, which is observed in the oil-saturated BN sample. Observation from both TEM and XRD studies compels us to conclude that there is no shift of the (0002) peak due to oil intercalation. Instead, the broad peak at 18° observed in XRD patterns of oil–saturated BN nanostructures originates from a characteristic length scale in the oil itself, as observed in x-ray diffraction of liquid samples[43], and is not associated with any changes to the BN aerogel structure. Due to the excessive amount of oil in the porous BN materials, the diffraction intensity of the (0002) peak of the BN is overwhelmed by the scattering from oil. We attribute the high oil uptake strictly to high surface area and pore volume. The BN aerogels presented here exhibit lower surface area (about 400 m^2/g compared to 1400 m^2/g), comparable pore size (20-50 nm) and slightly higher mesopore volume (1.29 vs. 1.09 cm^3/g) than the previously studied porous BN materials[6]. If the oil uptake were solely due to surface adsorption, one would expect an over three-fold decrease in the oil-uptake observed, whereas the BN aerogel oil-uptake capacity is only lower by 50%. If it were due to pore volume, a slight increase would be expected for the BN aerogels. Therefore, it appears that both surface adsorption and pore filling (mechanisms (i) and (ii) from above) play dominant roles in the oil uptake mechanism.

To determine the penetrability of non-aqueous liquids into the BN aerogel throughout the body of the aerogel sample, we take advantage of the adsorptive nature of the BN surface. Different

food dyes are dissolved in ethanol and the aerogels are submerged in the solutions for several hours and then dried. As seen in Fig. 6c, BN aerogels are capable of adsorbing dye molecules and displaying a dramatic change in color. The original BN aerogel is white in color (far left), and after dyeing, it carries the color of the dyes. Samples that have been broken open display the same color uniformly throughout the monolith (Fig. 6c, far right). This capacity for absorbing non-aqueous liquids into the pores of the BN aerogel, combined with its ability to be regenerated by burning in air, could make it a useful material for quick and effective environmental clean-up.

Conclusions

In summary, BN aerogels exhibit highly crystalline turbostratic structures with pure B-N bonding and mesopores formed by the wrapping of BN sheets. The nanoscale structure, chemistry, and mechanical strength of the BN aerogels are characterized. Additionally, the porous structures create a rough surface, which contributes to superhydrophobicity and high oil uptake capacity of the material. The high crystallinity, chemical inertness, thermal stability, porous structure, and its regeneration ability under heat treatment make sp^2-bonded BN aerogels a promising candidate for many applications including high temperature capacitors, extreme environment sensors, catalytic cavities, biological assays, and waste absorbents.

Acknowledgement

This work was supported in part by the U.S. Department of Energy under Contract # DE-AC02-05CH11231 which provided for TEM and X-Ray characterization, including that performed at the National Center for Electron Microscopy, and RSoXS; the UC Lab Fees Research Program under award 12-LR-235323 which provided for graphene aerogel synthesis and BN aerogel precursors; by Lawrence Livermore National Laboratory under the auspices of the U.S.

Department of Energy under Contract DE-AC52-07NA27344, through LDRD award 13-LW-099 which provided for mechanical and NMR measurements, and by the Air Force Office of Scientific Research under Grant X10-8049-C which provided for SEM and contact angle measurements. W. M. and A. Z. received support from the Center of Integrated Nanomechanical Systems under NSF Grant EEC-0832819. The authors thank Peter Ercius for assistance with collecting high-resolution TEM images, Ye Tian for helping with contact angle measurements, Dohyung Kim for assisting with XRD measurements, and Peidong Yang for providing XRD access.

Notes and References

[a] Department of Physics, University of California at Berkeley, Berkeley, California 94720, USA

[b] Department of Materials Science and Engineering, University of California at Berkeley, Berkeley, California 94720, USA

[c] Center of Integrated Nanomechanical Systems, University of California at Berkeley, Berkeley, California 94720, USA

[d] Department of Chemistry, University of California at Berkeley, Berkeley, California 94720, USA

[e] Physical and Life Science Directorate, Lawrence Livermore National Laboratory, 7000 East Avenue, Livermore, California 94550, USA

[f] Advanced Light Source, Lawrence Berkeley National Laboratory, Berkeley, California 94720, USA

[g] Department of Polymer Science & Engineering, Conte Polymer Research Center, University of Massachusetts, Amherst, Massachusetts 01003, USA

[h] Materials Science Division, Lawrence Berkeley National Laboratory, Berkeley, California 94720, USA

[i] Kavli Energy NanoSciences Institute at the University of California, Berkeley and the Lawrence Berkeley National Laboratory, Berkeley, California 94720, USA

* Corresponding author: azettl@berkeley.edu

‡ These authors contributed equally.

† Electronic Supplementary Information (ESI) available: High resolution TEM images of different portions of sample, photos of aerogels in oil bath over time, thermal gravimetric analysis data of the aerogels, and X – ray diffraction patterns of as – synthesized BN aerogels, oil – absorbed aerogels and oil droplet.

1 A. Corma, *Chem. Rev.*, 1997, **97**, 2373–2420.

2 P. Yang, D. Zhao, D. I. Margolese, B. F. Chmelka and G. D. Stucky, *Nature*, 1998, **396**, 152–155.

3 S. Inagaki, S. Guan, Y. Fukushima, T. Ohsuna and O. Terasaki, *J. Am. Chem. Soc.*, 1999, **121**, 9611–9614.

4 A. Stein, B. J. Melde and R. C. Schroden, *Adv. Mater.*, 2000, **12**, 1403–1419.

5 M. E. Davis, *Nature*, 2002, **417**, 813–21.

6 W. Lei, D. Portehault, D. Liu, S. Qin and Y. Chen, *Nat. Commun.*, 2013, **4**, 1777.

7 M. Rousseas, A. P. Goldstein, W. Mickelson, M. A. Worsley, L. Woo and A. Zettl, *ACS Nano*, 2013, **7**, 8540–6.

8 Q. Weng, X. Wang, C. Zhi, Y. Bando and D. Golberg, *ACS Nano*, 2013, **7**, 1558–65.

9 M. A. Worsley, S. O. Kucheyev, H. E. Mason, M. D. Merrill, B. P. Mayer, J. Lewicki, C. A. Valdez, M. E. Suss, M. Stadermann, P. J. Pauzauskie, J. H. Satcher, J. Biener and T. F. Baumann, *Chem. Commun. (Camb).*, 2012, **48**, 8428–30.

10 S. O. Kucheyev, A. V. Hamza, J. H. Satcher Jr. and M. A. Worsley, *Acta Mater.*, 2009, **57**, 3472–3480.

11 W. C. Oliver and G. M. Pharr, *J. Mater. Res.*, 2011, **7**, 1564–1583.

12 E. Gann, A. T. Young, B. A. Collins, H. Yan, J. Nasiatka, H. A. Padmore, H. Ade, A. Hexemer and C. Wang, *Rev. Sci. Instrum.*, 2012, **83**, 045110.

13 J. Ilavsky, *J. Appl. Crystallogr.*, 2012, **45**, 324–328.

14 M. A. Worsley, T. Y. Olson, J. R. I. Lee, T. M. Willey, M. H. Nielsen, S. K. Roberts, P. J. Pauzauskie, J. Biener, J. H. Satcher and T. F. Baumann, *J. Phys. Chem. Lett.*, 2011, **2**, 921–925.

15 M. J. McAllister, J.-L. Li, D. H. Adamson, H. C. Schniepp, A. A. Abdala, J. Liu, M. Herrera-Alonso, D. L. Milius, R. Car, R. K. Prud'homme and I. A. Aksay, *Chem. Mater.*, 2007, **19**, 4396–4404.

16 G. Moussa, C. Salameh, A. Bruma, S. Malo, U. Demirci, S. Bernard and P. Miele, *Inorganics*, 2014, **2**, 396–409.

17 J. Thomas, N. E. Weston and T. E. O'Connor, *J. Am. Chem. Soc.*, 1962, **84**, 4619–4622.

18 T. Sato, *Proc. Japan Acad. Ser. B Phys. Biol. Sci.*, 1985, **61**, 459–463.

19 P. S. Marchetti, D. Kwon, W. R. Schmidt, L. V. Interrante and G. E. Maciel, *Chem. Mater.*, 1991, **3**, 482–486.

20 C. Wang, D. H. Lee, A. Hexemer, M. I. Kim, W. Zhao, H. Hasegawa, H. Ade and T. P. Russell, *Nano Lett.*, 2011, **11**, 3906–11.

21 J. R. Tumbleston, B. A. Collins, L. Yang, A. C. Stuart, E. Gann, W. Ma, W. You and H. Ade, *Nat. Photonics*, 2014, **8**, 385–391.

22 B. A. Collins, J. E. Cochran, H. Yan, E. Gann, C. Hub, R. Fink, C. Wang, T. Schuettfort, C. R. McNeill, M. L. Chabinyc and H. Ade, *Nat. Mater.*, 2012, **11**, 536–43.

23 W.-Q. Han, H.-G. Yu and Z. Liu, *Appl. Phys. Lett.*, 2011, **98**, 203112.

24 L. J. Terminello, *J. Vac. Sci. Technol. A Vacuum, Surfaces, Film.*, 1994, **12**, 2462.

25 M. A. Worsley, S. Charnvanichborikarn, E. Montalvo, S. J. Shin, E. D. Tylski, J. P. Lewicki, A. J. Nelson, J. H. Satcher, J. Biener, T. F. Baumann and S. O. Kucheyev, *Adv. Funct. Mater.*, 2014, **24**, 4259–4264.

26 A. Nag, K. Raidongia, K. P. S. S. Hembram, R. Datta, U. V Waghmare and C. N. R. Rao, *ACS Nano*, 2010, **4**, 1539–44.

27 R. W. Pekala, C. T. Alviso and J. D. LeMay, *J. Non. Cryst. Solids*, 1990, **125**, 67–75.

28 W.-Q. Han, *Anisotropic Hexagonal Boron Nitride Nanomaterials: Synthesis and Applications*, Wiley-VCH Verlag GmbH & Co. KGaA, Weinheim, Germany, 2009.

29 G.-X. Li, Y. Liu, B. Wang, X.-M. Song, E. Li and H. Yan, *Appl. Surf. Sci.*, 2008, **254**, 5299–5303.

30 A. Pakdel, C. Zhi, Y. Bando, T. Nakayama and D. Golberg, *ACS Nano*, 2011, **5**, 6507–15.

31 A. R. Parker and C. R. Lawrence, *Nature*, 2001, **414**, 33–4.

32 L. B. Boinovich, A. M. Emelyanenko, A. S. Pashinin, C. H. Lee, J. Drelich and Y. K. Yap, *Langmuir*, 2012, **28**, 1206–16.

33 L. H. Li and Y. Chen, *Langmuir*, 2010, **26**, 5135–40.

34 C. H. Lee, J. Drelich and Y. K. Yap, *Langmuir*, 2009, **25**, 4853–4860.

35 J. Yu, L. Qin, Y. Hao, S. Kuang, X. Bai, Y.-M. Chong, W. Zhang and E. Wang, *ACS Nano*, 2010, **4**, 414–22.

36 Z. Li, Y. Wang, A. Kozbial, G. Shenoy, F. Zhou, R. McGinley, P. Ireland, B. Morganstein, A. Kunkel, S. P. Surwade, L. Li and H. Liu, *Nat. Mater.*, 2013, **12**, 925–31.

37 R. N. Wenzel, *Ind. Eng. Chem.*, 1936, **28**, 988–994.

38 A. B. D. Cassie and S. Baxter, *Trans. Faraday Soc.*, 1944, **40**, 546.

39 A. L. Ahmad, S. Sumathi and B. H. Hameed, *Chem. Eng. J.*, 2005, **108**, 179–185.

40 H.-P. Cong, X.-C. Ren, P. Wang and S.-H. Yu, *ACS Nano*, 2012, **6**, 2693–703.

41 K. Sohn, Y. Joo Na, H. Chang, K.-M. Roh, H. Dong Jang and J. Huang, *Chem. Commun. (Camb).*, 2012, **48**, 5968–5970.

42 Q. Zhu, Q. Pan and F. Liu, *J. Phys. Chem. C*, 2011, **115**, 17464–17470.

43 A. H. Narten, *J. Chem. Phys.*, 1977, **67**, 2102.

Table 1. Time evolution of water contact angle (WCA) of BN aerogels after different treatements (see main text).

	Anneal in Ar at 700 °C	Anneal in Ar at 800 °C	Anneal in air 700 °C	UV – ozone 15 mins	UV – ozone 60 mins	UV – ozone 90 mins
0 mins	150	148	87.5	98	82	59.8
20 mins	153	150	89.4	100	88	68.5
30 mins		152	90	105	88	82
90 mins		155	93	115	89	84
24 hrs	155	156	94	122	89.6	88
48 hrs		156	96	124	92	91
96 hrs		156	98	125	93	92

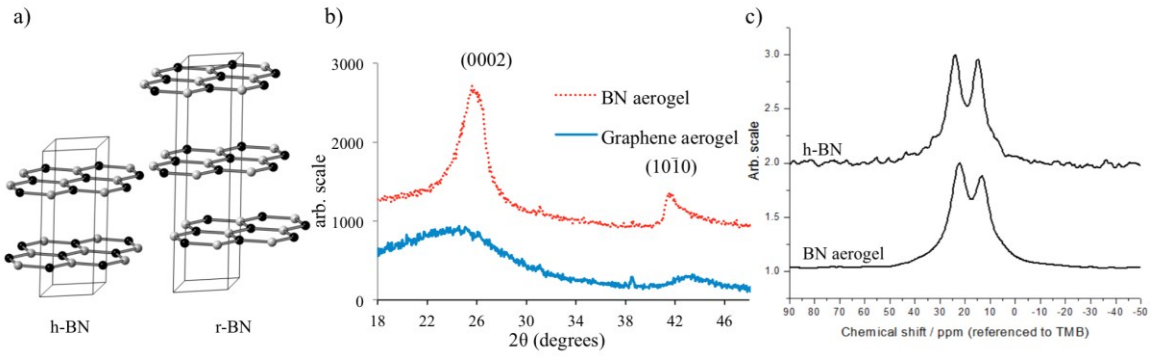

Fig. 1 a) Selected atoms from crystal structure models of hexagonal BN and rhombohedral BN, where boron atoms are black and nitrogen atoms are white. b) XRD patterns of graphene aerogel (lower, blue line) and BN aerogel (upper, red line), which is offset for clarity. Miller indices shown are for h-BN. c) Stack plot showing the solid-state ^{11}B spectra of h-BN and the BN aerogel.

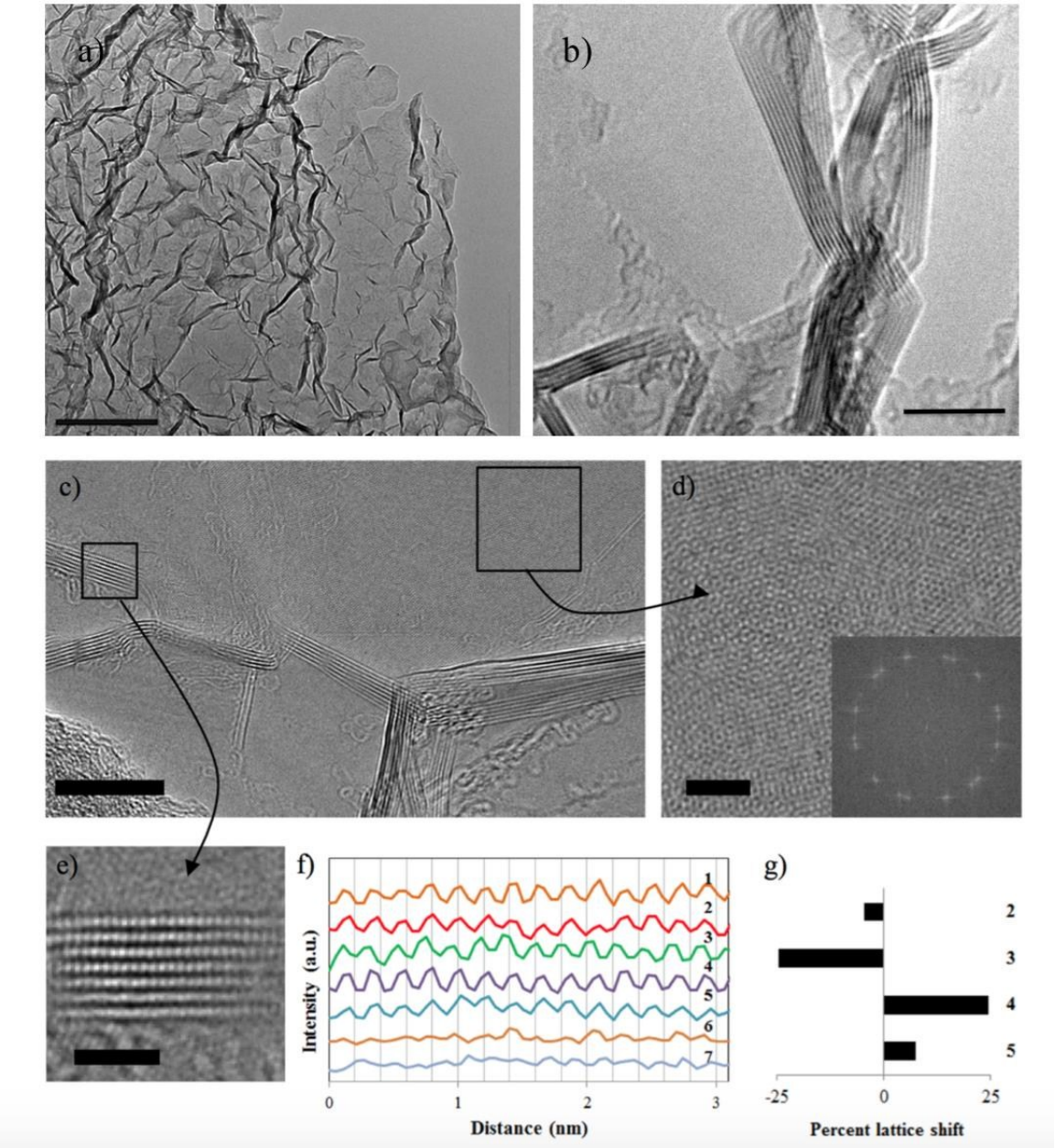

Fig. 2 (a – b) Low magnification TEM images of as-synthesized BN aerogels. Porosity and crystallinity are clearly seen. (c) TEM of a portion of the BN aerogel and (d) a magnified region of the image in part c, showing a portion of BN sheets lying parallel to the imaging plane. Inset: FFT of this region. (e) Another magnified region of the image in part c, where the BN layers lie perpendicular to the imaging plane. (f) Plot of grayscale intensity through the center of each of

the layers in part e, and (g) the average shift in register of layers 2-5 each relative to the layer above it. Scale bars are: (a) 200 nm, (b, c) 10 nm, and (d, e) 2 nm.

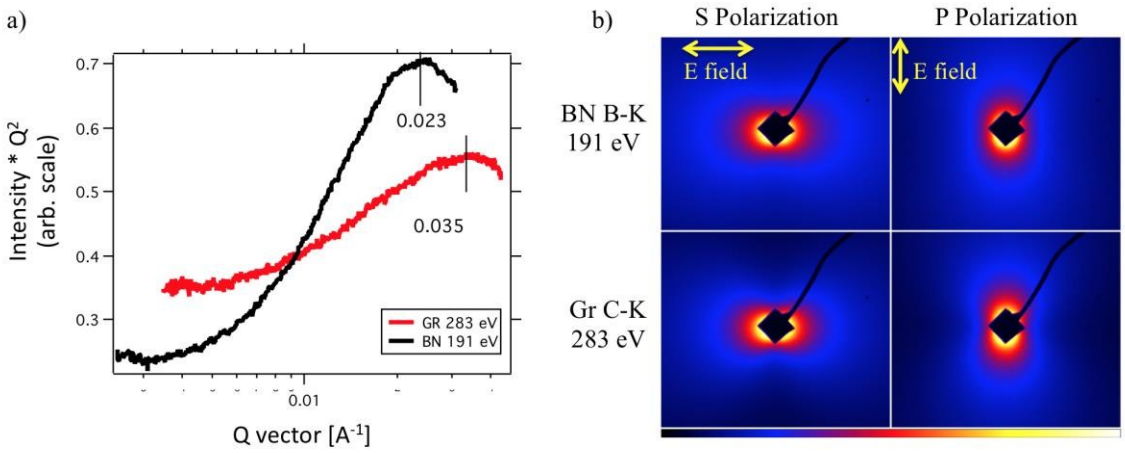

Fig. 3 a) Resonant soft X-ray scattering data for graphene (Gr) and BN aerogels. The scattering peaks correspond to pore size distribution. b) Scattering anisotropy of BN (upper) and graphene aerogels (lower) with X-rays at different polarizations (S and P) near the resonance energies of boron and carbon K-edges, respectively.

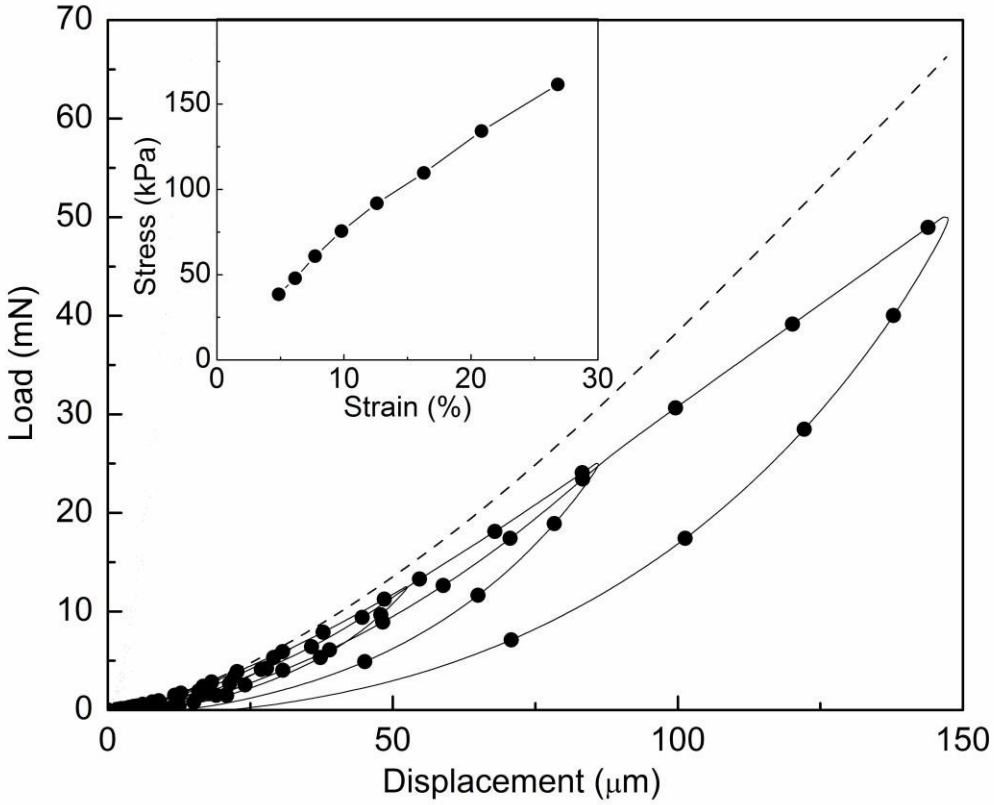

Fig. 4 Representative load-displacement curves of the BN aerogel. For clarity, only every 100th experimental point is depicted. The dashed line is a fit to the Hertzian model. Inset: indentation stress-strain curves of the aerogel.

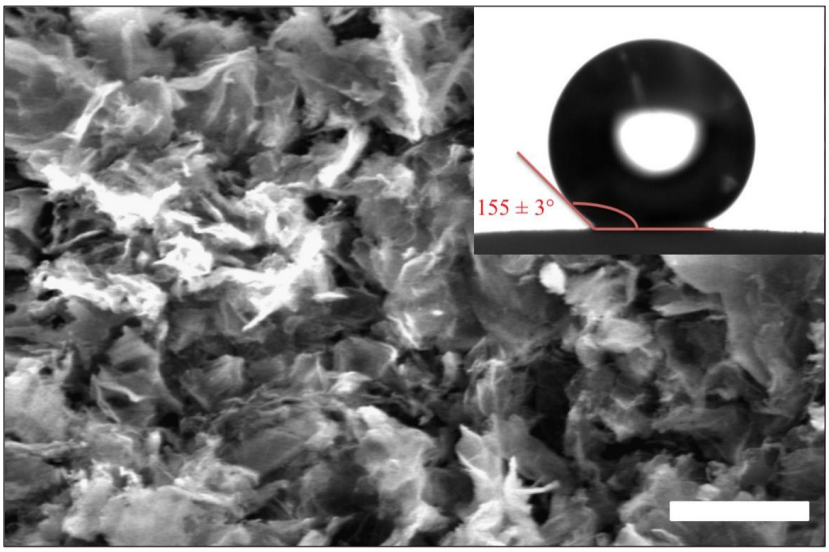

Fig. 5 SEM image of BN aerogel surface. Scale bar is 100 μm. Inset: Optical image of static water droplet on the BN aerogel surface.

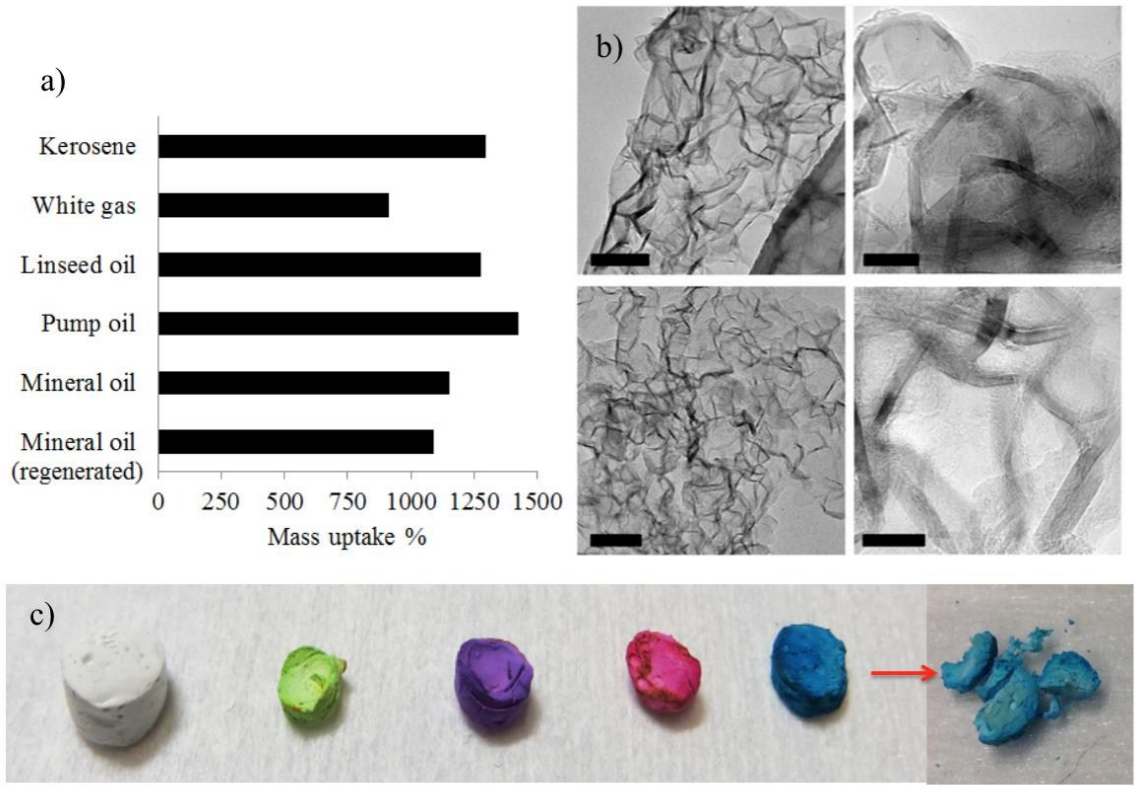

Fig. 6 (a) Mass uptake of the converted BN aerogels after 1 minute of soaking in various types of oils. (b) TEM images of the BN aerogels after calcining at 650 °C (top left and right, scale bars are 100 and 10 nm respectively) and after flame-burning (bottom left and right, scale bars are 50 and 10 nm respectively). (c) Photo of BN aerogel discs as-made (far left) and with absorbed dye, which penetrates though the aerogel (far right).

Table of content

This article studies the nanoscale structure of highly crystalline sp^2 – bonded boron nitride aerogels synthesized via carbothemic reduction from graphene aerogels, and its relationship to chemical and physical properties.